COMMUNICATION

Check for updates

A Ta$_3$N$_5$/BN composite for enhanced photocatalytic water splitting

Yao Xu, Haifeng Wang, Jiaming Zhang, Zihao Zhang, Meng Liu, Xiaowei Tao, Jifang Zhang* and Guijun Ma [iD]*

Narrow-bandgap Ta$_3$N$_5$ nanorods were supported on a BN substrate to produce a composite photocatalyst using NH$_4$Cl-based vacuum nitridation. The charge separation efficiency of Ta$_3$N$_5$ was effectively enhanced due to electron transfer from Ta$_3$N$_5$ to the BN substrate, boosting both the photocatalytic water oxidation and Z-scheme overall water splitting reactions.

Solar energy conversion into clean hydrogen resources through a photocatalytic process is a promising strategy for sustainable energy systems.[1,2] However, the development of efficient photocatalysts is constrained by limitations in light harvesting, especially in the visible region that makes up 45% of the solar spectrum,[3] and photon conversion efficiency, restrained by serious bulk and surface charge recombinations.[4–8] Ta$_3$N$_5$ has emerged as a particularly promising photocatalyst due to its bandgap of only 2.1 eV. The conduct band minimum (CBM) and valence band maximum (VBM) of Ta$_3$N$_5$ are composed of Ta 5d and N 2p orbitals, respectively, thermodynamically allowing for both photocatalytic and photoelectrochemical water redox reactions.[9,10] In 2002, Hitoki *et al.* reported photocatalytic water oxidation on Ta$_3$N$_5$ in the presence of an electron acceptor.[11] However, subsequent studies have demonstrated that the performance of Ta$_3$N$_5$ is fundamentally limited by issues directly stemming from the synthesis method. Specifically, Ta$_3$N$_5$ is typically prepared through an NH$_3$-based thermal nitridation process, which meets challenges including the formation of low-valence metal ions and O$_N$ anti-site defects within the crystal structure. These intrinsic defects act as recombination centers that severely suppress the charge separation efficiency.[12,13] Furthermore, high temperature duration leads to particle agglomeration of the products, exacerbating charge recombination issues. As a consequence of these synthesis-related challenges, Ta$_3$N$_5$ exhibits unsatisfactory photon conversion efficiencies in photocatalytic reactions.[14–16]

School of Physical Science and Technology, ShanghaiTech University, Shanghai 201210, China. E-mail: zhangjf3@shanghaitech.edu.cn, magj@shanghaitech.edu.cn

Nanostructural engineering, by precisely controlling the morphology and architecture of oxide precursors, has emerged as an effective strategy to improve the charge separation efficiency in Ta$_3$N$_5$ photocatalysts by reducing the charge transport distances and extending the carrier lifetimes.[17] Ma *et al.* applied a Ta$_2$O$_5$ and Na$_2$CO$_3$ mixture to produce a NaTaO$_3$/Ta$_2$O$_5$ composite, which was then used as a precursor for thermal ammonolysis. This method suppressed Ta$_3$N$_5$ agglomeration and enhanced the crystallinity.[14] Wang *et al.* prepared Ta$_2$O$_5$-coated Pt/SiO$_2$ nanoparticles for the fabrication of hollow Ta$_3$N$_5$ nanoshells, and subsequently loaded CoO$_x$ onto the outer surface of Ta$_3$N$_5$ with Pt left on the inner shell after removing SiO$_2$.[18] The nanoshell structure not only provided a structural framework for efficient charge transport but also facilitated directional carrier extraction by spatially separating the reduction and oxidation cocatalysts, thus boosting charge separation. Wang *et al.* applied KTaO$_3$ as a vaporous Ta resource to produce Ta$_3$N$_5$ nanorod single crystals and accelerate heating of the ammonium flow, which reduced the duration of the nitridation process. The highly crystallized Ta$_3$N$_5$ nanorods with fewer defects realized one-step excitation in the overall water splitting reaction under visible light illumination.[9] Nanostructured precursors enable controlled Ta$_3$N$_5$ particle morphology, effectively decreasing agglomeration and shortening the carrier transport distances, while structuring the catalyst/host interface promotes more efficient carrier transport, enhancing the charge separation efficiency and thereby unlocking Ta$_3$N$_5$'s potential for photocatalysis.

Our group has developed a NH$_4$Cl-based vacuum nitridation method to synthesize transition metal (oxy)nitrides such as a Ta$_3$N$_5$/Ta thin film,[19] TaON powders[20] and ZnO:GaN nanoparticles.[21,22] For the preparation of the Ta$_3$N$_5$/Ta thin film, only a Ta wafer and NH$_4$Cl were used as precursors. Upon heating, in the first step, NH$_3$ and HCl are produced from the decomposition of NH$_4$Cl. The metallic Ta reacts with HCl to produce a gaseous TaCl$_5$ intermediate, which subsequently reacts with NH$_3$ to form Ta$_3$N$_5$ particles on the surface of the Ta plate. The high permeability of the gaseous TaCl$_5$ and NH$_3$
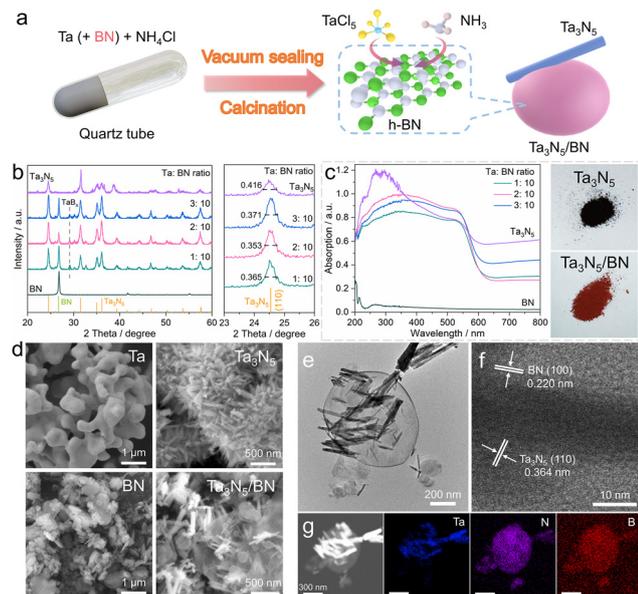
Fig. 1 (a) Illustration of the synthesis of the Ta_3N_5/BN composite. (b) XRD patterns of the BN precursor, bulk Ta_3N_5, and Ta_3N_5/BN samples prepared from different Ta/BN ratios. (c) UV-vis DRS of the BN, Ta_3N_5, and Ta_3N_5/BN powders, as well as digital images of the Ta_3N_5 and Ta_3N_5/BN (Ta : BN = 2 : 10) samples. (d) SEM images of the Ta and BN precursors and corresponding Ta_3N_5 and Ta_3N_5/BN products. (e) TEM, (f) HRTEM, and (g) dark field image and EDS mapping images of the Ta_3N_5/BN (Ta : BN = 2 : 10) sample. The referenced patterns of BN and Ta_3N_5 in (b) are ICDD-00-045-1171 and ICDD-04-004-4564, respectively.

reactants not only leads to rapid crystallization of the solid product but also prevents Ta_3N_5 from forming reduced Ta species by limiting exposure to an NH_3 atmosphere.

Herein, we introduce two-dimensional BN as a substrate for the growth of Ta_3N_5 nanoparticles in an NH_4Cl-based nitridation process. The involvement of BN in the precursor led to improved crystallinity and dispersion of the Ta_3N_5 particles. Reductive photodeposition of Ag and Rh suggested that electrons were transferred from Ta_3N_5 to BN under irradiation. Such directional charge migration greatly enhanced the photocatalytic activity of Ta_3N_5 for water splitting, highlighting the benefits of photocatalyst–substrate interaction.

The Ta_3N_5 bulk and Ta_3N_5/BN composite were synthesized by vacuum sealing a mixture of NH_4Cl and metallic Ta powder in a quartz tube with or without adding BN (Fig. 1a, with details shown in the SI). For Ta_3N_5/BN, the atomic ratios of Ta : BN were set as 1 : 10, 2 : 10 and 3 : 10, respectively. Fig. 1b displays the X-ray diffraction (XRD) patterns of the powders prepared with different Ta : BN ratios. All the BN-containing samples exhibit patterns of mixed BN and Ta_3N_5 peaks, with a weak signal at ∼29° assigned to TaB_x impurities. The majority of the peaks of Ta_3N_5/BN are consistent with the standard Ta_3N_5 patterns, indicating the high purity of Ta_3N_5 in the obtained samples. No signals of metallic Ta are observed in the products. Additionally, the full-width half-maximum (FWHM) of the Ta_3N_5 (110) diffraction peaks in the Ta_3N_5/BN samples is lower than that of Ta_3N_5, indicating enhanced crystallinity of Ta_3N_5

when BN is present during synthesis. Fig. 1c shows the UV-vis diffuse reflectance spectroscopy (DRS) of the BN, Ta_3N_5 and Ta_3N_5/BN powders. The BN precursor exhibits negligible UV-visible light absorption due to its wide bandgap of 5.1 eV. The Ta_3N_5 reference powder shows a broad absorption up to 600 nm corresponding to its bandgap (2.1 eV). The observed dark brown color, as opposed to dark red, can be attributed to elevated absorption in the near-infrared region. All of the Ta_3N_5/BN samples exhibit smooth band-to-band absorption features typical of Ta_3N_5, revealing that the optical properties of Ta_3N_5 did not change with the introduction of BN into the precursor, as corroborated by the Tauc plots in Fig. S1. Compared to Ta_3N_5, the relatively lower background levels above 600 nm for the Ta_3N_5/BN samples suggest less absorption associated with intragap defect states. Notably, the Ta : BN = 2 : 10 sample achieves the strongest light absorption, showing that photon absorption does not linearly increase with a higher Ta ratio in the precursor.

The scanning electron microscopy (SEM) images (Fig. 1d) display the morphology of the precursors and the nitridation products. Without incorporating BN during nitridation, large Ta precursor particles are converted into aggregated Ta_3N_5 nanorods. In the presence of BN, the nitridation products show more uniformly distributed and well-isolated Ta_3N_5 particles dispersed on the BN substrate. The SEM images of the different Ta_3N_5/BN samples (Fig. S2) in back scattered electron (BSE) mode show that the dispersity of the Ta_3N_5 nanorods in the Ta : BN = 2 : 10 sample is higher than that in the 1 : 10 and 3 : 10 samples. This demonstrates that the Ta content effectively impacts the growth of Ta_3N_5 particles, highlighting NH_4Cl-based vacuum nitridation as a potential method for constructing regulated nanostructures. The transmission electron microscopy (TEM) image of the Ta : BN = 2 : 10 sample (Fig. 1e) shows Ta_3N_5 nanorods with lengths around hundreds of nanometers lying on the BN substrate. The BN structure remains unchanged after the high-temperature nitridation. The TEM image clearly demonstrates that the Ta_3N_5 particles in the obtained samples adopt a typical nanorod morphology, which is similar to the Ta_3N_5 particles prepared directly from $TaCl_5$ and NH_3 precursors.[23] The high-resolution TEM (HRTEM) image in Fig. 1f exhibits the interface of the Ta_3N_5 and BN particles. The close stacking of the 0.364 nm lattice fringes assigned to the (110) facet of Ta_3N_5 and the 0.220 nm lattice fringes assigned to the BN (100) facet suggests the growth of Ta_3N_5 on the BN substrate. Fig. 1g shows the TEM dark field image and energy dispersive X-ray spectroscopy (EDS) of the Ta : BN = 2 : 10 sample. The overlapped N and Ta signals further confirm the nanorod morphology of Ta_3N_5 on the BN substrate.

XPS analysis was carried out on the Ta_3N_5, BN and Ta_3N_5/BN particles. The well-defined double peaks at 25.2 and 27.1 eV (Fig. 2a) assigned to Ta $4f_{7/2}$ and $4f_{5/2}$ in Ta_3N_5 reveal that the NH_4Cl-based nitridation suppresses the formation of reduced Ta species. For the Ta_3N_5/BN particles, additional double peaks are observed at high field shift, which are supposed to be TaO_x impurities.[24] The O 1s spectrum (Fig. S3) reveals the existence of crystalline O species in Ta_3N_5 and Ta_3N_5/BN, suggesting
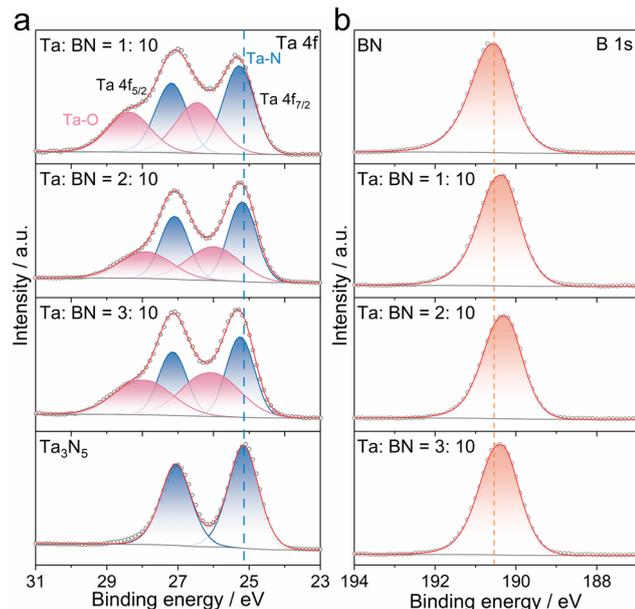
Fig. 2 XPS of the Ta₃N₅/BN samples prepared from different precursor ratios, including Ta₃N₅ and BN for reference. (a) Ta 4f and (b) B 1s spectra.

Fig. 3 HRTEM images and lattice fringe distances of the Ag particles loaded on (a) Ta_3N_5 and (b) BN in the Ta_3N_5/BN particles. (c) Dark field image, EDS mappings and structure diagram of the Ta_3N_5/BN sample loaded with Ag. (d) Transient absorption spectrum for Ta_3N_5 and Ta_3N_5/BN in water without (top panel) or with L-ascorbic acid (bottom panel). The pump and probe lights in (d) are 355 and 580 nm, respectively. The Ta_3N_5/BN sample is prepared from a Ta : BN = 2 : 10 ratio.

surface coverage of the TaO_x species. Besides, compared with Ta_3N_5, a slightly higher binding energy of the Ta^{5+} signals in Ta–N of the Ta_3N_5/BN samples reflects a possible electron transfer from Ta_3N_5 to BN. Relative to BN, the lower shift in B 1s binding energy for the Ta_3N_5/BN samples also suggests an interfacial electron transfer between the two components (Fig. 2b).

To verify electron transfer between Ta_3N_5 and BN under illumination, visible light-driven photoreduction of Ag^+ ions was performed, and Ag particles were loaded on the Ta_3N_5/BN composite photocatalyst. The 0.200 nm lattice fringes attributed to the Ag (103) facet are observed on both the BN and Ta_3N_5 particles. The EDS mappings in Fig. 3c clearly distinguish the Ag nanoparticles loaded away from the Ta_3N_5 nanorods. Considering that BN barely absorbs visible light, this indicates that photogenerated electrons are partially transferred from Ta_3N_5 to BN, as illustrated in the structure diagram of Fig. 3c. As further evidence, by using Rh^{3+} as a precursor, Rh nanoparticles can also be reductively photodeposited on the BN substrate (Fig. S4). Mott–Schottky analysis and valence spectra (Fig. S5) reveal that the Fermi level of BN is closely aligned with that of Ta_3N_5. Such energetic alignment is beneficial for electron transfer from Ta_3N_5 to BN.

Transient absorption spectroscopy was employed to investigate the electron transfer from Ta_3N_5 to BN under light excitation and in solution. The pump and probe lights were set at 355 and 580 nm, respectively. For BN alone (Fig. S6), no meaningful transient absorption signal is observed as its band gap exceeds the pump light wavelength. In contrast, both Ta_3N_5 and Ta_3N_5/BN show a weak negative absorption at 580 nm (Fig. 3d). To assign this signal, L-ascorbic acid is added as a hole scavenger. Here, the intensity of the negative absorption increases for both samples, confirming that this signal is associated with
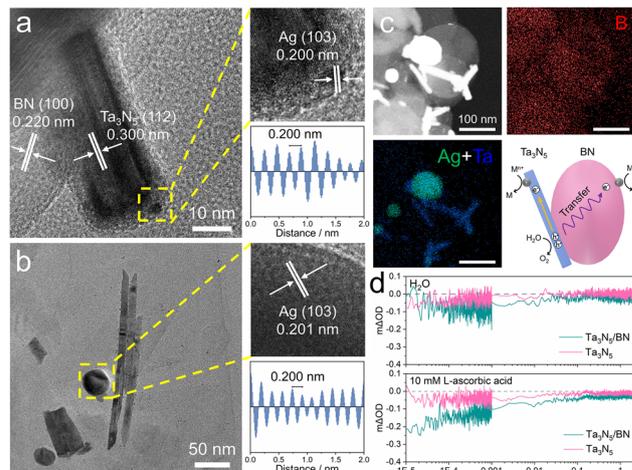
photogenerated electrons. It is worth noting that the negative absorption for Ta_3N_5/BN is significantly stronger than that for Ta_3N_5, indicating superior charge carrier separation in the former sample.

The catalyst–substrate electron transfer in Ta_3N_5/BN is supposed to promote its photocatalytic performance *via* improving electron–hole separation. Fig. 4a displays the activities of the photocatalytic oxygen evolution reaction (OER) on Ta_3N_5 or
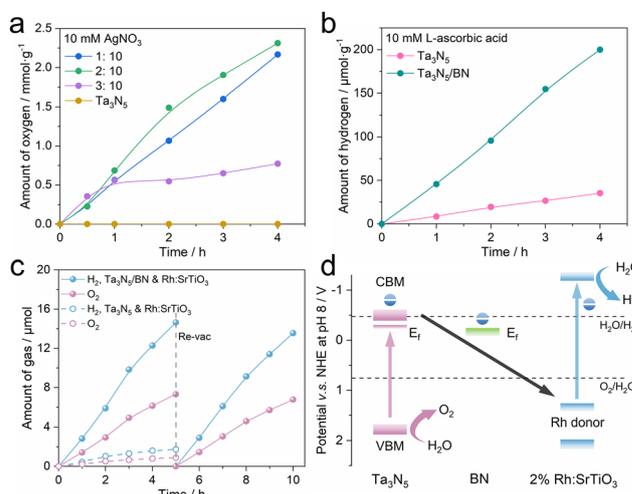

Fig. 4 (a) Time profiles of photocatalytic OER on Ta_3N_5/BN and bulk Ta_3N_5 samples in $AgNO_3$ reagent. (b) HER activities of Ta_3N_5/BN and Ta_3N_5 in L-ascorbic acid reagent. (c) H_2 and O_2 production from physical oscillation between Ta_3N_5/BN and 2% $Rh:SrTiO_3$ at pH 5. (d) Diagram of Z-scheme electron transfer between Ta_3N_5/BN and $Rh:SrTiO_3$. The Ta_3N_5/BN in (b) and (c) are prepared from a Ta : BN = 2 : 10 ratio and each assessment applied 30 mg of catalyst. 0.75 wt% IrO_2 and 1 wt% Pt were loaded as cocatalysts for OER and HER, respectively.

Ta_3N_5/BN in the presence of $AgNO_3$ as an electron scavenger. An IrO_2 species is loaded on the catalysts to assist the OER process (Fig. S7). The Ta_3N_5 nanorods barely produce oxygen due to rapid passivation by Ag coverage on their active sites.[23] However, Ta_3N_5/BN exhibits linear oxygen evolution in the early stages, revealing that electron interaction slows down the Ag passivation and preserves the photocatalytic activity. Among the Ta_3N_5/BN products, the Ta : BN = 2 : 10 sample has the highest water oxidation rate. This is likely due to better photon absorption (Fig. 1c) and the more uniform distribution of Ta_3N_5 nanorods on the BN substrate (Fig. S2) for this sample.

Fig. 4b displays photocatalytic hydrogen evolution (HER) on Ta_3N_5/BN (Ta : BN = 2 : 10) and Ta_3N_5 assisted with L-ascorbic acid as a hole sacrificial reagent. Pt (1 wt%) is optimized as the HER cocatalyst (Fig. S7). The Ta_3N_5/BN composite structure also shows a considerably enhanced hydrogen evolution rate compared with Ta_3N_5 nanorods, although it remains much lower than the OER rate. This highlights the thermodynamic limitations of Ta_3N_5/BN for proton reduction (Fig. S8). To break such limitations, Fig. 4c displays a Z-scheme overall water splitting reaction by physical collision between Ta_3N_5/BN and Rh-doped $SrTiO_3$ (Rh:$SrTiO_3$) particles. Under visible light illumination, stoichiometric hydrogen and oxygen evolution over 10 h is realized for Ta_3N_5/BN, while the Ta_3N_5 exhibits significantly lower activity. Fig. 4d represents the band structure of Ta_3N_5/BN and Rh:$SrTiO_3$ determined from Mott–Schottky and bandgap assessment in Fig. S9. It is obvious that transfer of photogenerated electrons from Ta_3N_5 to BN favors the Z-scheme electron transfer pathway, effectively overcoming the insufficient reduction driving force of Ta_3N_5/BN.

In summary, a Ta_3N_5/BN composite photocatalyst is synthesized *via* the NH_4Cl-based vacuum nitridation process. The Ta_3N_5 component exhibits highly crystallized nanorod morphology during growth on the BN substrate. Photodeposition of Ag metal, chemical state analysis and carrier dynamics assessment confirmed electron transfer between Ta_3N_5 and BN. Enhanced photocatalytic performance in water splitting emphasizes the promotion of the charge separation efficiency by electron interaction at the catalyst/substrate interface. Our work not only provides a new method for synthesizing highly crystallized Ta_3N_5 nanorods but also demonstrates an efficient composite structure for enhancing the photocatalytic performance of this promising photocatalyst.

Conflicts of interest

There are no conflicts to declare.

Data availability

The data supporting this article have been included as part of the supplementary information (SI). Supplementary information is available. The detailed SEM images, XPS spectra, experiment conditions were displayed in supplementary information. See DOI: **https://doi.org/10.1039/d5cc03833b**.

Notes and references

1 W. Wang, X. Xu, W. Zhou and Z. Shao, *Adv. Sci.*, 2017, **4**, 1600371.
2 Q. Yang, X. Tong and Z. Wang, *Mater. Rep.: Energy*, 2024, **4**, 100253.
3 Q. Wang and K. Domen, *Chem. Rev.*, 2020, **120**, 919–985.
4 Q. Wang, C. Pornrungroj, S. Linley and E. Reisner, *Nat. Energy*, 2021, **7**, 13–24.
5 S. Ye, W. Shi, Y. Liu, D. Li, H. Yin, H. Chi, Y. Luo, N. Ta, F. Fan and X. Wang, *et al.*, *J. Am. Chem. Soc.*, 2021, **143**, 12499–12508.
6 M. S. Prévot and K. Sivula, *J. Phys. Chem. C*, 2013, **117**, 17879–17893.
7 J. H. Kim, J. W. Jang, Y. H. Jo, F. F. Abdi, Y. H. Lee, R. van de Krol and J. S. Lee, *Nat. Commun.*, 2016, **7**, 13380.
8 L. Pan, J. H. Kim, M. T. Mayer, M.-K. Son, A. Ummadisingu, J. S. Lee, A. Hagfeldt, J. Luo and M. Grätzel, *Nat. Catal.*, 2018, **1**, 412–420.
9 Z. Wang, Y. Inoue, T. Hisatomi, R. Ishikawa, Q. Wang, T. Takata, S. Chen, N. Shibata, Y. Ikuhara and K. Domen, *Nat. Catal.*, 2018, **1**, 756–763.
10 Y. Q. Xiao, C. Feng, J. Fu, F. Z. Wang, C. L. Li, V. F. Kunzelmann, C. M. Jiang, N. Nakabayashi, N. Shibata and I. D. Sharp, *et al.*, *Nat. Catal.*, 2020, **3**, 932–940.
11 G. Hitoki, A. Ishikawa, T. Takata, J. N. Kondo, M. Hara and K. Domen, *Chem. Lett.*, 2002, 736–737.
12 G. Fan, T. Fang, X. Wang, Y. Zhu, H. Fu, J. Feng, Z. Li and Z. Zou, *iScience*, 2019, **13**, 432–439.
13 J. Fu, F. Wang, Y. Xiao, Y. Yao, C. Feng, L. Chang, C.-M. Jiang, V. F. Kunzelmann, Z. M. Wang and A. O. Govorov, *et al.*, *ACS Catal.*, 2020, **10**, 10316–10324.
14 S. S. Ma, T. Hisatomi, K. Maeda, Y. Moriya and K. Domen, *J. Am. Chem. Soc.*, 2012, **134**, 19993–19996.
15 K. N. Sun, Y. Y. Li, Q. G. Zhang, L. Wanga, J. L. Zhang and X. Zhou, *Appl. Surf. Sci.*, 2017, **405**, 289–297.
16 X. Wang, H. Huang, G. Fan, Z. Li and Z. Zou, *J. Phys. Chem. C*, 2017, **122**, 489–494.
17 M. Xiao, S. C. Wang, S. Thaweesak, B. Luo and L. Z. Wang, *Engineering*, 2017, **3**, 365–378.
18 D. Wang, T. Hisatomi, T. Takata, C. Pan, M. Katayama, J. Kubota and K. Domen, *Angew. Chem., Int. Ed.*, 2013, **52**, 11252–11256.
19 Y. Xiang, B. Zhang, J. Liu, S. Chen, T. Hisatomi, K. Domen and G. Ma, *Chem. Commun.*, 2020, **56**, 11843–11846.
20 Y. Xu, K. Liu, J. Zhang, B. Zhang, J. Zhang, K. Shi, H. Wang and G. Ma, *J. Energy Chem.*, 2024, **94**, 541–550.
21 K. Liu, B. Zhang, J. Zhang, W. Lin, J. Wang, Y. Xu, Y. Xiang, T. Hisatomi, K. Domen and G. Ma, *ACS Catal.*, 2022, 14637–14646, DOI: **10.1021/acscatal.2c04361**.
22 K. Liu, B. Zhang, J. Zhang, Y. Xu, J. Zhang, Z. Zhang, K. Shi, N. Wang, S. Chen and G. Ma, *ACS Catal.*, 2024, **14**, 10138–10147.
23 D. L. Lu, M. Hara, T. Hisatomi, T. Takata and K. Domen, *J. Phys. Chem. C*, 2009, **113**, 17151–17155.
24 M. Li, W. Luo, D. Cao, X. Zhao, Z. Li, T. Yu and Z. Zou, *Angew. Chem., Int. Ed.*, 2013, **52**, 11016–11020.